Conference on Modelling Fluid Flow (CMFF'25)
The 19th International Conference on Fluid Flow Technologies
Budapest, Hungary, August 26-August 29, 2025

Enhancing DEM-CFD Simulations with Machine-Learning-Based Locally Resolved Nusselt Number Correlations

Ali Mjalled[1], Bo Jaeger[2], Reza Namdar[3], Lucas Mieg[1], Enric Illana[2], Fathollah Varnik[3], Viktor Scherer[2], Martin Mönnigmann[1]

[1] Automatic Control and Systems Theory, Ruhr-Universität Bochum. E-mails: {ali.mjalled, lucas.mieg, martin.moennigmann}@ruhr-uni-bochum.de
[2] Energy Plant Technology, Ruhr-Universität Bochum. E-mails: {jaeger, illana, scherer}@leat.ruhr-uni-bochum.de
[3] Interdisciplinary Centre for Advanced Materials Simulation. E-mails: {Reza.Namdarkedenji, fathollah.varnik}@ruhr-uni-bochum.de

ABSTRACT

Accurate prediction of heat transfer between solid particles and the surrounding gas is essential in discrete element method - computational fluid dynamics (DEM-CFD) simulations. Typically, these methods rely on empirical correlations of the Nusselt number (Nu) that provide only an averaged estimation of the heat transfer between the particles and the fluid. In light of this, we present in this paper a data-driven surrogate model that captures the local heat transfer on the particle surface and integrates it into the DEM-CFD simulation framework. The developed model is a Gaussian process (Nu-GP) that is trained using a database of 16 2D direct numerical simulations (DNS) of convective heat-transfer in air flow around an isolated circular particle with Reynolds numbers in the range $100 \leq \mathrm{Re} \leq 400$. The model uses the inlet Reynolds number and the local radial angle θ on the surface of the particle as inputs to predict the local Nusselt number. Comparisons to the DNS results demonstrate the ability of the Nu-GP to accurately predict the local Nusselt within the trained range. Furthermore, we show the Nu-GP model can be integrated into DEM-CFD and resolves the heat transfer on the particle surface with DNS accuracy with a negligible increase of computational cost compared to mean Nusselt correlations.

Keywords: DEM-CFD, Gaussian processes, lattice Boltzmann, Nusselt number

NOMENCLATURE

A	$[m^2]$	area
D	$[m]$	particle diameter
F	$[N]$	force
M_w	$[kg/mol]$	molecular weight
N_y, N_z	$[-]$	number of grid points
R	$[J/kg \cdot mol]$	universal gas constant
T	$[K]$	temperature
Nu	$[-]$	Nusselt number
Pr	$[-]$	Prandtl number
Re	$[-]$	Reynolds number
$\mathcal{D}$	$[-]$	training dataset
$\mathcal{K}$	$[-]$	GP covariance
$\mathcal{N}$	$[-]$	Gaussian distribution
c_p	$[J/kg \cdot K]$	specific heat capacity
l	$[m]$	length
p	$[-]$	probability
p_h	$[Pa]$	hydrodynamic pressure
p_t	$[Pa]$	thermodynamic pressure
$\underline{\underline{I}}$	$[-]$	identity matrix
$\underline{\underline{X}}$	$[-]$	training input matrix
$\underline{u}$	$[m/s]$	velocity
$\underline{x}$	$[-]$	training input vector
$\underline{y}$	$[-]$	training output vector
$\underline{\epsilon}$	$[-]$	noise
λ	$[W/m \cdot K]$	thermal conductivity
μ	$[Pa \cdot s]$	dynamic viscosity
ρ	$[kg/m^3]$	density
σ^2	$[-]$	variance
θ	$[^\circ]$	radial angle
$\underline{\phi}$	$[-]$	GP hyperparameters vector
$\underline{\underline{\tau}}$	$[Pa]$	viscous stress tensor
ε	$[-]$	porosity
ξ	$[-]$	GP mean

Subscripts and Superscripts

ref, surf	reference, surface
opt	optimal solution
b	body
t	time
$\bar{(\cdot)}$	spatial mean

1. INTRODUCTION

Particle-resolved direct numerical simulations (DNS) enable accurate predictions of heat transfer between solid particles and surrounding gas. These simulations require a finely resolved computational grid, at least an order of magnitude smaller than the (average) diameter of the particles. However, the substantial computational cost of DNS renders its application to flow fields in packed-bed configurations infeasible for many real-world scenarios. Instead, such systems are typically simulated using non-particle-resolved approaches, such as the discrete element method coupled with computational fluid dynamics (DEM-CFD) [1].

The computational cells in DEM-CFD are typically larger than the individual particles. Therefore, the heat transfer within the cell is approximated using spatially averaged values. To account for thermal effects, empirical correlations of the Nusselt (Nu) number are employed [2, 3]. While this approach enables faster simulations, it comes at the cost of reduced accuracy compared to DNS. To bridge this gap, the use of locally resolved Nusselt correlations in DEM-CFD has been proposed that provide more detailed thermal information within the computational cell [4]. Although many studies have investigated the local heat transfer at the particle surface [5, 6], relatively few have derived local models or correlations.

Notably, Haeri and Shrimpton [7] derived a correlation for the calculation of the local Nusselt number around a circular cylinder using trigonometric series with 13 coefficients. Each series is modelled as a 5th order polynomial in Reynolds (Re) and Prandtl (Pr) numbers within the ranges $10 \leq \mathrm{Re} \leq 250$ and $0.1 \leq \mathrm{Pr} \leq 40$. Similarly, Kravets and Kruggel-Emden [8] investigated local heat transfer and provided Nusselt correlations corresponding to Pr = 1 for forced convection around an isolated sphere and random particle packings. Their correlations are applicable from low to moderate Reynolds numbers, i.e., $20 \leq \mathrm{Re} \leq 240$ for the single particle case, and $20 \leq \mathrm{Re} \leq 100$ for the packed-bed corresponding to porosity ε ranging from 0.6 and 1.0. To the best of our knowledge, no further local Nusselt number models or correlations for flow fields around solid bodies have been reported in the literature. Yet, we note that the local correlations have been developed in related applications, such as the local Nusselt correlations for circular impinging jet over a plate [9], and for nanofluids in circular horizontal tubes [10].

While the majority of heat transfer studies have relied on nonlinear regression to fit power-law Nusselt correlations, other machine learning methods have been also explored. For example, Urbina et al. [10] employed genetic programming to discover non-trivial local Nusselt correlations for nanofluids. Kahani et al. [11] used artifical neural networks and support vector machines to predict the average Nusselt number for TiO_2/water nanofluid flows. Similarly, Panda et al. [12] applied polynomial regression, random forest, and artifical neural networks to model average Nusselt values in heat exchanger with twisted tape inserts. More recently, Sanhueza et al. [13] utilized convolutional neural network to create detailed 2D maps of the local Nusselt number in turbulent flows over rough surfaces.

Despite recent advances, there remains a clear shortage in the literature regarding local Nusselt number correlations, especially for fluid flow around solid bodies. Accordingly, we aim in this work to develop a local Nusselt correlation using Gaussian processes (GP), which is, to the best of our knowledge, the first application of this machine learning method in this context. Specifically, we extend the Reynolds number range of the local correlations proposed by Haeri and Shrimpton [7] up to Re = 400 with a fixed Pr = 0.7. We aim to include our trained and validated GP within the DEM-CFD framework to obtain a locally resolved heat transfer on the particle surface in a non-particle-resolved framework.

The paper is organized as follows. Section 2 presents the DNS model. In Sec. 3, we derive the local and average Nusselt number correlations. Section 4 presents the DEM-CFD model with simulation results based on the derived local correlations. Conclusions and an outlook are stated in Sec. 5.

2. DNS SIMULATION SETUP AND DATA GENERATION

This section outlines the mathematical framework and numerical approach employed in the DNS, which are used to generate the database of the surrogate model. The simulations investigate convective heat transfer around a stationary circular particle, with air as the working fluid, over a range of Reynolds numbers.

2.1. Governing Equations

The flow and heat transfer are modeled using a thermal, compressible formulation under the low Mach number approximation. This allows for density variations driven by temperature changes, beyond the Boussinesq approximation. The governing equations include conservation of mass, momentum, and energy, and are given by

$$\partial_t \rho + \underline{\nabla} \cdot (\rho \underline{u}) = 0, \tag{1}$$

$$\partial_t (\rho \underline{u}) + \underline{\nabla} \cdot (\rho \underline{u} \otimes \underline{u}) = -\underline{\nabla} p_h + \underline{\nabla} \cdot \underline{\underline{\tau}} + \underline{F}_\mathrm{b}, \tag{2}$$

$$\rho c_p (\partial_t T + \underline{\nabla} \cdot \underline{u} T) = -\underline{\nabla} \cdot (\lambda \underline{\nabla} T) + \partial_t p_t, \tag{3}$$

$$\rho = \frac{p_t M_w}{RT}, \tag{4}$$

where, ρ, $\underline{u}$, p_h, $\underline{\underline{\tau}}$, and $\underline{F}_\mathrm{b}$ represent the gas density, velocity field, hydrodynamic pressure, viscous stress tensor, and body force per unit volume, respectively. T, c_p, λ, p_t, M_w, and R denote the temperature, specific heat at constant pressure, thermal conductivity, thermodynamic pressure, molecular weight, and the universal gas constant, respectively.

To capture the thermal expansion effects, the velocity divergence is computed from a combination of the continuity equation and the ideal gas law. Assuming a constant pressure, this yields

$$\underline{\nabla} \cdot \underline{u} = -\frac{1}{\rho}\frac{D\rho}{Dt} = \frac{1}{T}\frac{DT}{Dt}. \tag{5}$$

The dynamic viscosity is temperature-dependent and modeled using Sutherland's law

$$\mu(T) = \mu_{\text{ref}}\left(\frac{T}{T_{\text{ref}}}\right)^{3/2}\frac{T_{\text{ref}} + S}{T + S}, \tag{6}$$

where $\mu_{\text{ref}} = 1.68 \times 10^{-5} Pa \cdot s$, $T_{\text{ref}} = 273K$, and $S = 110.5K$ are reference values specific to air. With a fixed Prandtl number (Pr = 0.7), the thermal conductivity is computed as $\lambda = \mu c_p/\text{Pr}$. Local and average Nusselt numbers are defined as

$$\text{Nu}_i = \frac{D\,\lambda\,\frac{\partial T_i}{\partial n}\big|_{\text{surf}}}{\lambda_0(T_{\text{surf}} - T_{\text{inlet}})}, \tag{7}$$

$$\overline{\text{Nu}} = \frac{1}{A}\int_A \text{Nu}\, dA, \tag{8}$$

where λ and λ_0 are the gas thermal conductivities, respectively, calculated at surface temperature of cylinder and mean temperature $T_0 = (T_{\text{surf}} + T_{\text{inlet}})/2$. The symbol A represents the lateral surface area of the particle. In a discrete treatment, (8) can be approximated as $\overline{\text{Nu}} = \sum \text{Nu}_i/n_{\text{nodes}}$, where n_{nodes} denotes the total number of surface nodes and Nu_i the local Nusselt number. The temperature gradients (7) are approximated using a first-order-accurate finite-difference (FD) scheme, tuned to ensure that the total heat transfer matches the one computed between the inlet and outlet boundaries.

The above equations are solved using a hybrid numerical approach. Specifically, the lattice Boltzmann method (LBM) [14] is employed for solving the flow field, while the temperature field is evolved using a FD scheme. The reader is referred to Hosseini et al. [15] for more details related to the hybrid LBM-FD formulation.

2.2. Simulation setup

The simulations are conducted in a two-dimensional domain representing the flow of air around a stationary circular cylinder. The inlet boundary is subjected to a uniform velocity and temperature of $300K$, while the cylinder surface is held at a constant temperature of $301K$. Although the model is capable of accounting for thermal expansion effects, the temperature difference is deliberately kept small to suppress such influences and facilitate direct comparison with prior studies in the literature. No-slip boundary conditions are applied on the particle, with periodic boundaries along the lateral edges and a convective outflow condition at the outlet.

We consider Reynolds numbers in the range $\text{Re} \in [100, 400]$, defined based on the particle diameter D, inlet velocity, and inlet kinematic viscosity. Grid independence and time-step sensitivity analyses are performed to ensure accuracy. The convective and diffusive terms in the finite-difference method are discretized using a second-order central scheme, while the time integration employs a first-order explicit Euler scheme.

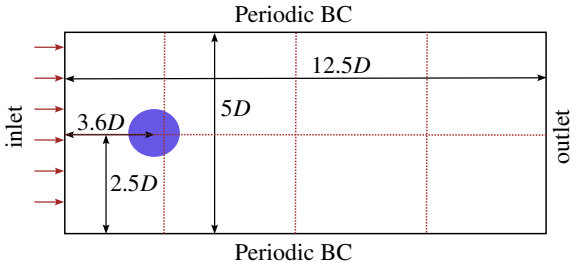

Figure 1. Schematic view of simulation setup. The red dashed lines denote the domain discretization used for the DEM-CFD simulation. D denotes the particle diameter.

After an initial transient period, the flow evolves into a repetitive pattern characterised by vortex shedding – commonly referred to as a Kármán vortex street. To avoid a bias from transient dynamics, the computation of the local Nusselt number is performed after the initial transient stage. These results on the local Nusselt number serve as the primary quantities of interest for thermal analysis and subsequent machine learning applications.

A sketch of the computational domain, including boundary conditions and geometric proportions, is shown in Figure 1. Additional details regarding the simulation parameters and flow properties are listed in Table 1, where N_y and N_z denote the total number of grid points along the lateral, y, and flow, z, directions, respectively (see Fig. 5 for the corresponding directions).

Table 1. Simulation parameters used in the study

Parameters	Values
Grid Size $[mm^2]$	0.0625
M_w $[kg/mol]$	0.02896
N_z, N_y	500, 200
c_p $[J/kg \cdot K]$	1005
Time Step $[s]$	4.0×10^{-4}

2.3. Model validation

In Fig. 2, we compare the local distribution of the Nusselt number with numerical benchmark results. Specifically, we compare our results to Kim & Choi [16] for Re = 120 and to Momose & Kimoto [17] and Zhang et al. [18] for Re = 218. The results show generally good agreement, with the LB-FD solver capturing the overall trend of the local Nusselt number distribution. However, minor discrepancies are observed, which can be attributed to the numerical model used. Specifically, LBM cannot achieve an orthogonal grid resolution with re-

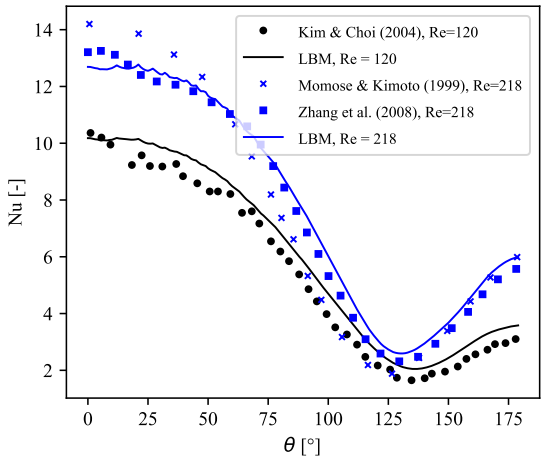

Figure 2. Validation of the model. The results are compared with Kim & Choi [16] for Re = 120 and Momose & Kimoto [17] and Zhang et al. [18] for Re = 218. The angle $\theta = 0°$ corresponds to the stagnation point of the flow.

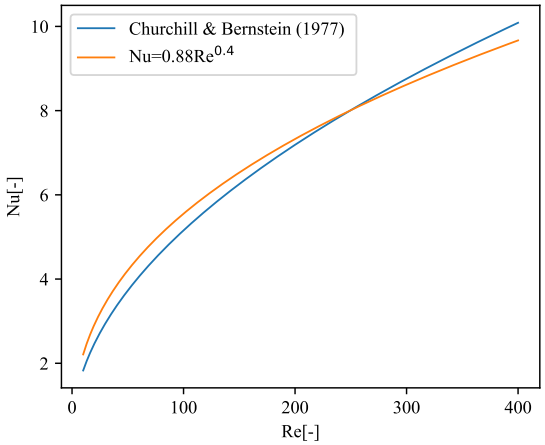

Figure 3. Comparison of steady-state average Nusselt values as function of the Reynolds number, based on (9) and Churchill & Bernstein's correlation (10).

spect to solid surfaces, requiring specialized treatments for curvature. In this study, a linear second-order bounce-back scheme is applied to approximate the exact position of the solid surface. While this approach yields reasonable results, some discrepancies may still arise due to the approximations in the representation of the boundary.

2.4. Average correlation

We fit an average steady-state Nusselt correlation using the available DNS database, in order to benchmark our results against established correlations from the literature. The resulting equation is given by

$$\overline{\mathrm{Nu}} = 0.88\mathrm{Re}^{0.4}. \tag{9}$$

Note that (9) does not depend on Pr number, as the training data are obtained from simulations with constant Pr = 0.7. We compare our results to Churchill & Bernstein's correlation for forced convection from gases and liquids to a circular cylinder in crossflow [19], which reads

$$\overline{\mathrm{Nu}} = 0.3 + \frac{0.62\,\mathrm{Re}_D^{1/2}\,\mathrm{Pr}^{1/3}}{\left[1 + (0.4/\mathrm{Pr})^{2/3}\right]^{1/4}} \times \left[1 + \left(\frac{\mathrm{Re}_D}{282\,000}\right)^{5/8}\right]^{4/5}. \tag{10}$$

The results are plotted in Fig. 3 for the range Re = [20, 400]. The two correlations show very good agreement, even in the range Re = [20, 100[that was not included during training. Overall, the maximum deviation is $\Delta\mathrm{Nu} \approx 0.48$ and occurs at Re = 40. This corresponds to a relative error of $\approx 14\%$.

3. LOCAL AND AVERAGE NUSSELT CORRELATIONS

3.1. Gaussian process regression

We consider a set of N training data points $\mathcal{D} = \{\underline{x}_i, \mathrm{Nu}_i\}_{i=1}^N$, where each $\underline{x} = [\mathrm{Re}, \theta]^T \in \mathcal{X} \subset \mathbb{R}^2$ denotes the input feature vector composed of the inlet Reynolds number and the local radial angle at the particle surface. The corresponding output Nu_i is obtained with (7). We note that the local Nusselt number values from each simulation are calculated by averaging the local values over all time steps after the transient phase. The start of this post-transient regime is identified by the appearance of the von Kármán vortex street in the wake of the cylinder.

We train a regression model $f : \mathcal{X} \to \mathbb{R}$ that maps the input feature vector $\underline{x}$ to the local Nusselt number on the particle surface for the configuration presented in Sec. 2. Since multiple regression functions may fit the data equally well, we adopt a Gaussian process (GP) prior over f, which provides distribution over functions and enables uncertainty quantification in the predictions. By definition, a GP is a collection of random variables, any finite number of which have a joint Gaussian distribution [20]. We assume that the prior of f is a GP and

$$f(\underline{x}) \sim \mathcal{GP}(\xi(\underline{x}), \mathcal{K}(\underline{x}, \underline{x}')), \tag{11}$$

where $\xi(\underline{x})$ is the mean function and $\mathcal{K}(\underline{x}, \underline{x}')$ is the covariance (or kernel) function describing the correlation between any pair of inputs $\underline{x}$ and $\underline{x}'$. The mean function $\xi(\underline{x})$ is chosen to be constant and equal to the mean of the training set. For the covariance function, we adopt a radial basis function (RBF) kernel, which is defined as

$$\mathcal{K}(\underline{x}, \underline{x}')) = \sigma_c^2 \exp\left(-\frac{(\mathrm{Re} - \mathrm{Re}')^2}{2l_{\mathrm{Re}}^2} - \frac{(\theta - \theta')^2}{2l_\theta^2}\right), \tag{12}$$

where σ_c^2 is the signal variance and $l_{(\cdot)}$ is the length scale of the corresponding input. These variables are treated as hyperparameters of the model.

Although our training data is generated from DNS, it is common in GPs to take measurement errors into consideration. Accordingly, we assume that the training outputs are corrupted by additive Gaussian noise $\epsilon \sim \mathcal{N}(0, \sigma_n^2)$, i.e.,

$$\mathrm{Nu}_i = f(\underline{x}_i) + \epsilon, \quad i = 1, \cdots, N, \tag{13}$$

where σ_n^2 is the noise variance and is considered as an additional hyperparameter.

Let $\mathcal{T} = \{\underline{x}_m^*\}_{m=1}^M$ be a collection of M test points, with each $\underline{x}_m^* = [\mathrm{Re}^*, \theta_m^*]^T$ comprising a new Reynolds number value, i.e., not used in the training dataset $\mathcal{D}$, and a local test angle θ_m^* on the particle surface. The goal is to predict the corresponding local Nusselt number at these test points. In GP regression, the joint distribution of the training outputs $\underline{y} = [\mathrm{Nu}_1, \cdots, \mathrm{Nu}_N]^T$ and the test outputs $\underline{y}^* = [\mathrm{Nu}_1^*, \cdots, \mathrm{Nu}_M^*]^T$ is a multivariate Gaussian. According to the conditional Gaussian theorem [21], the predictive distribution for $\underline{y}^*$, conditioned on the training data $(\underline{\underline{X}}, \underline{y})$ and test inputs $\underline{\underline{X}}^*$ is given by

$$p(\underline{y}^* | \underline{\underline{X}}, \underline{y}, \underline{\underline{X}}^*) = \mathcal{N}(\tilde{\xi}, \tilde{\mathcal{K}}), \tag{14}$$

where $\underline{\underline{X}}, \underline{\underline{X}}^*$ are the matrices of training and testing input features, respectively. Here, $\tilde{\xi}$ and $\tilde{\mathcal{K}}$ denote the mean and covariance of the posterior predictive distribution, and they are obtained using

$$\tilde{\xi} = \xi(\underline{\underline{X}}^*) + \mathcal{K}(\underline{\underline{X}}^*, \underline{\underline{X}}) \left(\mathcal{K}(\underline{\underline{X}}, \underline{\underline{X}}) + \sigma_n^2 \underline{\underline{I}} \right)^{-1} (\underline{y} - \xi(\underline{\underline{X}})), \tag{15}$$

$$\tilde{\mathcal{K}} = \mathcal{K}(\underline{\underline{X}}^*, \underline{\underline{X}}^*) - \mathcal{K}(\underline{\underline{X}}^*, \underline{\underline{X}}) \left(\mathcal{K}(\underline{\underline{X}}, \underline{\underline{X}}) + \sigma_n^2 \underline{\underline{I}} \right)^{-1} \mathcal{K}(\underline{\underline{X}}, \underline{\underline{X}}^*). \tag{16}$$

The hyperparameters of the GP, i.e., $\underline{\phi} = [\sigma_c^2, \sigma_n^2, l_{\mathrm{Re}}, l_\theta]^T$, have a strong influence on the prediction accuracy; therefore, they must be optimized. This is accomplished by maximizing the log-likelihood of training outputs $\underline{y}$ given the inputs $\underline{\underline{X}}$ and hyperparameters $\underline{\phi}$, i.e.,

$$\underline{\phi}_{\mathrm{opt}} = \underset{\underline{\phi}}{\mathrm{argmax}} \log(p(\underline{y} | \underline{\underline{X}}, \underline{\phi})), \tag{17}$$

where

$$\log(p(\underline{y} | \underline{\underline{X}}, \underline{\phi})) = -\frac{1}{2} \left(\underline{y} - \xi(\underline{\underline{X}}) \right)^T \left(\mathcal{K}(\underline{\underline{X}}, \underline{\underline{X}}) + \sigma_n^2 \underline{\underline{I}} \right)^{-1} \left(\underline{y} - \xi(\underline{\underline{X}}) \right) - \frac{1}{2} \log \left| \mathcal{K}(\underline{\underline{X}}, \underline{\underline{X}}) + \sigma_n^2 \underline{\underline{I}} \right| - \frac{N}{2} \log(2\pi). \tag{18}$$

The gradients of the log-likelihood with respect to every hyperparameter can be computed analytically. Therefore, the optimization problem shown in (17) can be efficiently solved using gradient-based optimization methods, e.g., L-BFGS [22] or conjugate gradient methods.

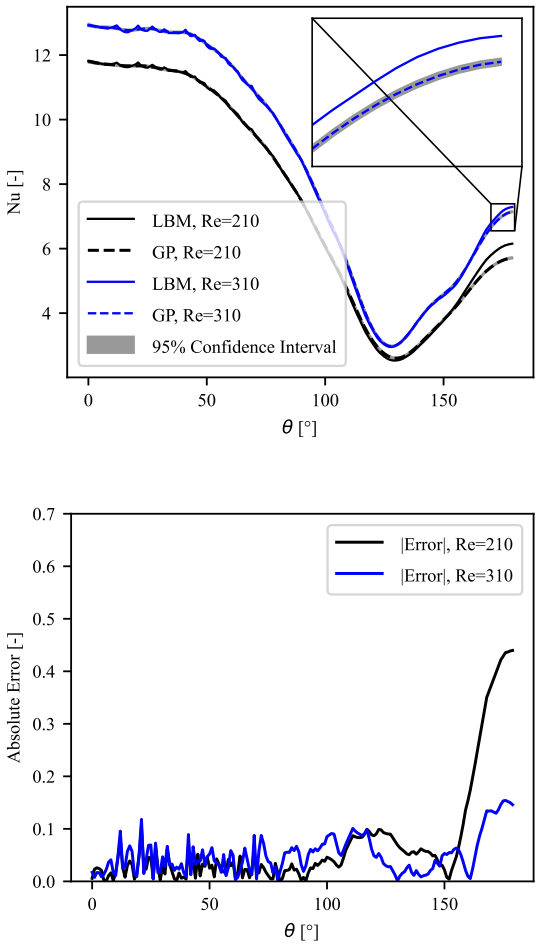

Figure 4. Top: GP evaluation for two test cases with Re = 210 and 310 with 95% confidence intervals. Bottom: Corresponding absolute prediction error. The angle $\theta = 0°$ corresponds to the stagnation point of the flow.

Once the hyperparameters have been optimized using $\mathcal{D}$, the GP model can be used for inference on an unseen test inputs by evaluating the posterior distribution according to Eqs. (14) to (16).

3.2. Training setup

Our training dataset $\mathcal{D}$ consists of 5760 training samples obtained by computing the local Nusselt number at every 1° increment along the particle surface, with 0° corresponding to the stagnation point. These values are extracted from 16 DNS simulations, each parameterized by a distinct inlet Reynolds number uniformly distributed in the range $[100, 400]$. In addition, we scale the input features of $\mathcal{D}$ between 0 and 1 to improve the numerical conditioning of the kernel matrix.

The hyperparameters $\underline{\phi}$ are optimized using the

L-BFGS algorithm provided by Scikit-learn [23]. We restart the optimization using 10 different initializations in the hyperparameter space to avoid poor local minima. The resulting optimal hyperparameter vector, identified using the scaled inputs, is $\underline{\phi} = [32.376, 1.71 \times 10^{-4}, 0.542, 0.01]^T$.

3.3. Gaussian Process model evaluation

We evaluate the accuracy of the model by comparing the local Nusselt values, predicted by the GP, to the ground truth values obtained from the DNS simulations for the test cases with Re = 210, 310. The corresponding root mean square errors (RMSE) are 0.14 and 0.09, respectively. Figure 4 shows the angular distribution of Nusselt number along the particle surface for the two considered test cases, along with the corresponding absolute prediction error. The results show that the GP is capable of accurately predicting the local Nusselt number values over the entire angular range, with near-perfect agreement except in the wake region behind the cylinder, where it slightly underestimates the Nusselt values. The reason for this discrepancy lies in the complex flow behavior in the wake region, where flow separation effects dominate. Specifically, the GP predicts temporally averaged local Nusselt values learned from the training data, which may not fully capture the influence of Reynolds number on the target values in this region. Moreover, the shaded gray region, which represents the 95% confidence interval, is extremely narrow, indicating high certainty in the predictions.

4. LOCALLY RESOLVED DEM-CFD SIMULATIONS

4.1. GP implementation in DEM-CFD framework

Gaussian Process DEM-CFD simulations for the setup described in Sec. 2.2 were carried out using the in-house DEM-CFD-code. We refer to [24, 25] for more details on the code. Here we focus on the integration of the GP into the DEM-CFD framework and highlight the benefits of using local Nusselt number model. First, to mimic the numerical conditions of unresolved 3D-DEM-CFD simulations, the fluid domain was deliberately meshed with a coarse grid consisting of (1x2x4) cells. This configuration ensures that the particle size remains much smaller than the CFD size $L_{\text{CFD, cell}}$, i.e., $L_{\text{CFD, cell}} \gg D$. Furthermore, only one cell constitutes the domain depth (x-direction) to enforce a quasi-2D flow configuration, which is comparable to the DNS setup. The grid of the fluid domain used is depicted in Fig. 1 with red dashed lines.

In the DEM approach, the particles are represented as polyhedra [26] with a discretized (triangulated) surface. This polyhedron representation has two advantages: First, any particle shape can be included and the local approach can later be easily translated to other particle shapes. Second, boundary conditions from the triangulated surface mesh can easily be translated to adjacent cells of an intra-particle tetrahedral mesh. The radial surface discretization of the circular particle is depicted in Fig. 5. We note that the particle depth is discretized using only one cell, analogous to the fluid domain.

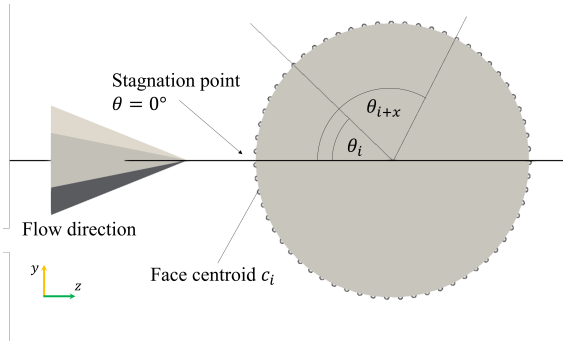

Figure 5. Radial discretization of the circular particle.

Our implementation of the GP within the DEM-CFD framework provides the Nu number distribution along the particle surface at every 1°, based on the inlet Reynolds number, which is readily available in the simulation. However, to project this distribution onto the particle faces in the DEM-CFD domain and assign the local Nusselt number Nu_θ, it is necessary to first identify the stagnation point on the particle surface ($\theta = 0°$). This is achieved by comparing the orientation of each particle face to the flow vector $\underline{u}$ obtained from the CFD solution. Once the stagnation point is known, the remaining θ_i are calculated during runtime from the face centroids c_i and the corresponding values of Nu_θ are assigned on the respective faces.

4.2. Results

The advantages of using the GP-Nu in DEM-CFD are obvious: While the simulation is unresolved ($L_{\text{CFD, cell}} \gg D$) and, therefore, local information of the fluid-solid heat transfer is not available, the GP provides Nu_θ on the particle surface with a DNS level of accuracy. This is particularly interesting if the external heat transfer is coupled to a resolved internal heat transport. An example of this is depicted in Fig. 6, which shows the temperature profiles of the disc for the locally resolved and mean case. It is evident from the temperature profiles that, due to the spatial resolution of Nusselt on the surface, the transient heat conduction inside the particle is more realistic than for a mean Nusselt value. As the Nusselt number at the stagnation point is the largest and drops to less than half its value on the back of the disc ($\theta > 90°$), the thermal front moving towards the disc core takes on a half-moon shape. Consequently, heat transfer in the particle is not uniformly directed towards the center of the particle as in the mean Nusselt case.

In Fig. 7, we compare the evolution of the mean

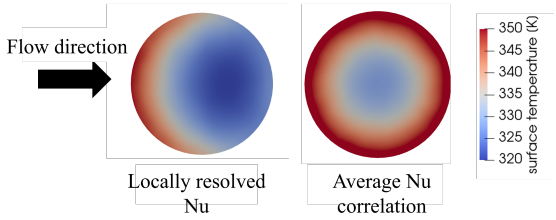

Figure 6. Temperature profiles at $t = 100s$, $T_{in} = 400K$ and Re = 100.

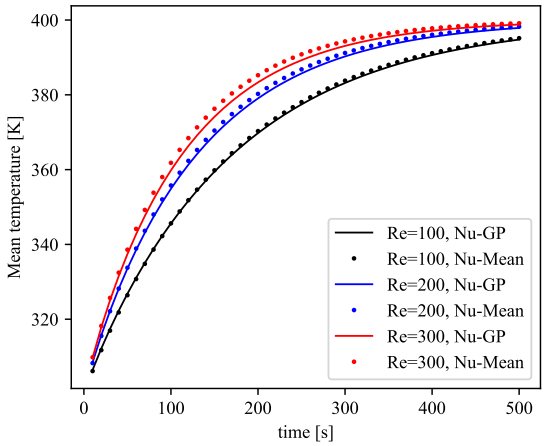

Figure 7. Temperature evolution for locally resolved GP DEM-CFD simulations and reference DEM-CFD for Re = 100, 200, 300.

particle temperature for the GP DEM-CFD model and the model that employs a mean Nusselt number for three different Reynolds numbers (Re = 100, 200, 300). As expected, the heating time of the particle is approximately the same for the two cases and the three respective Reynolds numbers, since the integral of Nu_θ (i.e. heat flux) in the GP case equals the mean Nusselt number value. Although mean temperatures are quite similar, temperature is not distributed radially uniform in the GP case, as shown before, and local surface temperature differences may lie in the range of $20 - 25K$ for the depicted cases.

Regarding the computational effort, the GP takes marginally more time to calculate the local Nu_θ, compared to using mean Nusselt values. This overhead is mainly attributed to computing a single Cholesky decomposition used for the matrix inversion given in Eqs. (15) and (16), which takes $\approx 3-4s$ to compute.

5. CONCLUSION

In this work, a local Gaussian process model for the Nusselt number (Nu-GP) has been presented. The GP was trained using a DNS database performed with the LBM to crossflow around an isolated circular cylinder, parameterized by Pr = 0.7 and $100 \leq \text{Re} \leq 400$. We first validated an LBM model against benchmark results from the literature, demonstrating good agreement with some deviations near the stagnation point. Subsequently, we trained a Gaussian Process to represent the LBM results at a low computational cost. The Gaussian Process achieves excellent accuracy on test cases when compared to the original LBM data, with a maximum RMSE of 0.14. Finally, we demonstrated that our GP-Nu can easily be integrated into a coupled DEM-CFD framework. We illustrated this integration with first GP-Nu DEM-CFD simulation results. Those show that GP-Nu models indeed provide locally resolved Nusselt numbers, while requiring only very little additional computational effort compared to mean Nusselt correlations.

The cylindrical particle case studied in this work constitutes a readily verifiable and thus essential step toward establishing a solid foundation for more complex particle geometries. This simplified scenario enables us to validate the approach before extending it to irregular shapes, which will require incorporating additional descriptors into the Gaussian Process model alongside Re and θ. In future work we aim to develop robust correlations that capture a broader spectrum of particle shapes and simulation setups, including cases involving denser particle packings.

ACKNOWLEDGEMENTS

Funded by the Deutsche Forschungsgemeinschaft (DFG, German Research Foundation) - Project-ID 422037413 - TRR 287.

REFERENCES

[1] Tsuji, Y., Kawaguchi, T., and Tanaka, T., 1993, "Discrete particle simulation of two-dimensional fluidized bed", *Powder Technology*, Vol. 77 (1), pp. 79–87.

[2] Gnielinski, V., 1976, "New equations for heat and mass transfer in turbulent pipe and channel flow", *International Chemical Engineering*, Vol. 16 (2), pp. 359–367.

[3] Wakao, N., and Kagei, S., 1982, *Heat and mass transfer in packed beds*, Vol. 1, Taylor & Francis.

[4] Sudbrock, F., Kruggel-Emden, H., Wirtz, S., and Scherer, V., 2015, "Convective drying of agitated silica gel and beech wood particle beds—experiments and transient DEM-CFD simulations", *Drying Technology*, Vol. 33 (15-16), pp. 1808–1820.

[5] Niazmand, H., and Renksizbulut, M., 2003, "Transient three-dimensional heat transfer from rotating spheres with surface blowing", *Chemical Engineering Science*, Vol. 58 (15), pp. 3535–3554.

[6] Kishore, N., and Ramteke, R. R., 2016, "Forced convective heat transfer from spheres to Newtonian fluids in steady axisymmetric flow regime

with velocity slip at fluid–solid interface", *International Journal of Thermal Sciences*, Vol. 105, pp. 206–217.

[7] Haeri, S., and Shrimpton, J., 2013, "A correlation for the calculation of the local Nusselt number around circular cylinders in the range $10 \leq \mathrm{Re} \leq 250$ and $0.1 \leq \mathrm{Pr} \leq 40$", *International Journal of Heat and Mass Transfer*, Vol. 59, pp. 219–229.

[8] Kravets, B., and Kruggel-Emden, H., 2017, "Investigation of local heat transfer in random particle packings by a fully resolved LBM-approach", *Powder Technology*, Vol. 318, pp. 293–305.

[9] Dhruw, L., Kothadia, H. B., and Rajagopal, A. K., 2023, "Local and area average Nusselt number correlation for a circular impinging jet over a flat plate", *Journal of Thermal Analysis and Calorimetry*, Vol. 148 (24), pp. 14031–14050.

[10] Guzman-Urbina, A., Fukushima, K., Ohno, H., and Fukushima, Y., 2023, "Deriving local Nusselt number correlations for heat transfer of nanofluids by genetic programming", *International Journal of Thermal Sciences*, Vol. 192, p. 108382.

[11] Kahani, M., Ahmadi, M. H., Tatar, A., and Sadeghzadeh, M., 2018, "Development of multilayer perceptron artificial neural network (MLP-ANN) and least square support vector machine (LSSVM) models to predict Nusselt number and pressure drop of TiO2/water nanofluid flows through non-straight pathways", *Numerical Heat Transfer, Part A: Applications*, Vol. 74 (4), pp. 1190–1206.

[12] Panda, J. P., Kumar, B., Patil, A. K., Kumar, M., and Kumar, R., 2023, "Machine learning assisted modeling of thermohydraulic correlations for heat exchangers with twisted tape inserts", *Acta Mechanica Sinica*, Vol. 39 (1), p. 322036.

[13] Sanhueza, R. D., Akkerman, I., and Peeters, J. W., 2023, "Machine learning for the prediction of the local skin friction factors and Nusselt numbers in turbulent flows past rough surfaces", *International Journal of Heat and Fluid Flow*, Vol. 103, p. 109204.

[14] Succi, S., 2001, *The lattice Boltzmann equation: for fluid dynamics and beyond*, Oxford University Press.

[15] Hosseini, S. A., Safari, H., Darabiha, N., Thévenin, D., and Krafczyk, M., 2019, "Hybrid lattice Boltzmann-finite difference model for low Mach number combustion simulation", *Combustion and Flame*, Vol. 209, pp. 394–404.

[16] Kim, J., and Choi, H., 2004, "An immersed-boundary finite-volume method for simulation of heat transfer in complex geometries", *KSME International Journal*, Vol. 18 (6), pp. 1026–1035.

[17] Momose, K., and Kimoto, H., 1999, "Forced convection heat transfer from a heated circular cylinder with arbitrary surface temperature distributions", *Heat Transfer—Asian Research: Co-sponsored by the Society of Chemical Engineers of Japan and the Heat Transfer Division of ASME*, Vol. 28 (6), pp. 484–499.

[18] Zhang, N., Zheng, Z., and Eckels, S., 2008, "Study of heat-transfer on the surface of a circular cylinder in flow using an immersed-boundary method", *International Journal of Heat and Fluid Flow*, Vol. 29 (6), pp. 1558–1566.

[19] Churchill, S. W., and Bernstein, M., 1977, "A correlating equation for forced convection from gases and liquids to a circular cylinder in cross-flow", *International Journal of Heat and Mass Transfer*.

[20] Williams, C. K., and Rasmussen, C. E., 2006, *Gaussian processes for machine learning*, Vol. 2, MIT Press Cambridge, MA.

[21] Murphy, K. P., 2012, *Machine learning: a probabilistic perspective*, MIT press.

[22] Liu, D. C., and Nocedal, J., 1989, "On the limited memory BFGS method for large scale optimization", *Mathematical Programming*, Vol. 45 (1), pp. 503–528.

[23] Pedregosa, F., Varoquaux, G., Gramfort, A., et al., 2011, "Scikit-learn: Machine Learning in Python", *Journal of Machine Learning Research*, Vol. 12, pp. 2825–2830.

[24] Illana Mahiques, E., Brömmer, M., Wirtz, S., and Scherer, V., 2023, "Locally Resolved Simulation of Gas Mixing and Combustion Inside Static and Moving Particle Assemblies", *Chemical Engineering & Technology*, Vol. 46 (7), pp. 1362–1372.

[25] Abdi, R., Jaeger, B., Illana, E., Wirtz, S., Schiemann, M., and Scherer, V., 2025, "Modelling of heat transfer in moving granular assemblies with a focus on radiation using the discrete ordinate method: A DEM-CFD approach", *Particuology*, Vol. 100, pp. 78–94.

[26] Höhner, D., Wirtz, S., and Scherer, V., 2012, "A numerical study on the influence of particle shape on hopper discharge within the polyhedral and multi-sphere discrete element method", *Powder Technology*, Vol. 226, pp. 16–28.